Detecting the gravitational wave memory effect with TianQin

Shuo Sun, Changfu Shi,* Jian-dong Zhang, and Jianwei Mei
MOE Key Laboratory of TianQin Mission, TianQin Research Center for Gravitational Physics & School of Physics and Astronomy, Frontiers Science Center for TianQin, Gravitational Wave Research Center of CNSA, Sun Yat-sen University (Zhuhai Campus), Zhuhai 519082, China

(Received 1 August 2022; revised 11 December 2022; accepted 4 January 2023; published 13 February 2023)

The gravitational wave memory effect is a prediction of general relativity. The presence of memory effect in gravitational wave signals not only provides the chance to test an important aspect of general relativity, but also represents a potentially non-negligible contribution to the waveform for certain gravitational wave events. In this paper, we study the prospect of detecting the gravitational wave memory effect directly with the planned space-based gravitational wave detector—TianQin. We find that during its five years of operation, for the gravitational wave signals that could be detected by TianQin, about 0.5–2.0 signals may contain displacement memory effect with signal-to-noise ratios (SNRs) greater than 3. This suggests that the chance for TianQin to detect the displacement memory effect directly is low but not fully negligible. In contrast, the chance to detect the spin memory is negligible. We also study that in which parameter space, the memory effect is expected to be significant in waveform modeling.

DOI: 10.1103/PhysRevD.107.044023

I. INTRODUCTION

The observations of gravitational waves (GWs) from binary black hole mergers [1–3] have opened a new window to observe the universe, which not only promise a deeper understanding of compact objects in the universe [4–6] but also provide a new way to test general relativity [7–9]. Both the detection of GWs and the testing of general relativity require accurate waveforms of GWs. Among all the contributions to the GW waveforms, the GW memory effect is particularly interesting not only in that it can potentially be directly observed and thus serves as an important test of general relativity, but also in that it depends on the entire past history of the gravitational systems [10,11].

Under real physical conditions, the spacetime background seen by an observer near the null infinity before and after a flux of GW radiation is not purely vacuum, but contains GW sources at a long distance. Due to the loss of energy and other conserved charges of the GW sources, the radiation of GWs typically leads to a permanent change to the spacetime, and this has been known as the *linear* memory effect since the early 1970s [12,13]. A second type of memory effect was later discovered by Christodoulou [14] and has been called the *nonlinear* memory effect, for it involves the contribution of the GW strain at the quadratic order. The Christodoulou effect does not appear as a change of the charges of the GW sources but is still related to the permanent change of the background spacetime. It has been suggested to rename the *linear* and *nonlinear* memory effect as the *ordinary* and *null* memory effect, respectively, to be more clear on what they truly represent [15].

Since the memory effect is a persistent change of the spacetime, it is natural to relate it to the symmetries and the corresponding charges that characterize different spacetimes (see [16] for some early references). However, it was only in the past few years that the relations among the various types of memory effect and the various types of Bondi-Metzner-Sachs (BMS) transformations [17–24] were elucidated and established [16,25–27]. Such understanding has enabled systematic calculations of the memory effect using the so called BMS flux-balance laws [27–32].

The detection of memory effect has attracted much attention in recent years. Attempts have been made to calculate the memory effect for cosmic strings [33] and core-collapse supernovae [34]. There have also been calculation of memory effect in alternative theories of gravitation, such as scalar tensor theory [35], Brans-Dicke theory [36,37] and Chern-Simons modified gravity [38]. Using the memory effect to test alternative theories of gravitation has also been studied, such as for the Brans-Dicke theory with screening [39].

The strategies for detecting the GW memory effect were first proposed by Braginsky and Thorne in the 1980s [13,40]. Since the first detection of GWs by LIGO in 2015 [41], many works about detecting memory effect with current and future GW detectors have appeared [30,42–56]. It has been found that the memory effect is difficult to

*Corresponding author.
shichf6@mail.sysu.edu.cn

detect directly with the current ground-based GW detectors, but the future ground-based detectors such as Cosmic Explorer [57] and Einstein Telescope [58] may be able to detect the memory effect [59]. The memory effect produced by the massive BBH systems can fall in the most sensitive frequency band of space-based detectors, and thus have better chance at revealing the memory effect with space-based detectors. Indeed, the prospect of detecting memory effect with the planned space-based GW detector LISA has been studied in [60], and it has been shown that LISA can directly detect the displacement memory from the merger of massive black hole binarys (MBHBs). It is also possible to detect memory effect with pulsar timing array [42–47].

TianQin is a space-based GW detector targeting GWs in the frequency band 10^{-4} Hz ~ 1 Hz [61,62]. Among the promising scientific discovery potential of TianQin in many different directions [63–74], the detection of MBHBs is an outstanding one [75,76]. Motivated by the known result on LISA, it is likely that TianQin can also detect memory effect directly. But the orbit, the constellation size and motion of TianQin are quite different from those of LISA, and so are the sensitive frequency band and the response of the detector to GWs. So it is necessary to study the related problems for TianQin independently, especially when it comes to the question of when the memory effect will become a must-consider factor during science and data analysis.

In this paper, we study the prospect of directly detecting the gravitational wave memory effect with TianQin and also determine the region of parameter space in which the contribution of memory effect is potentially non-negligible.

The paper is organized as following. In Sec. II, we recall the basic results on memory effect. In Sec. III, we introduce the calculation of memory corrections to the waveform. In Sec. IV, we study the potential of detecting memory effect directly with TianQin. In Sec. V, we study the parameter space in which the memory effect could become an adverse factor if not properly taken into consideration. Finally, we summarize in Sec. VI.

II. MEMORY EFFECT

In this section, we recall some of the basics of memory effect and the calculation of the corresponding waveform and we set $G = c = 1$. The purpose is to have all the relevant nomenclature clearly defined and to keep the logic in a self-contained manor. There is nothing particularly new in this section and we mainly follow the treatment and notation of [29,31].

Physically, there are three different types of memory effect: the displacement memory [12,13], which causes the relative displacement between two test masses to change after the passage of GWs, the spin memory [26], which causes the change in the relative time delay of two free-falling test masses that are initially on antiorbital trajectories, and the center-of-mass memory effect [16], which causes the change in the relative time delay of two free-falling test masses that are initially on antiparallel trajectories. All three types of memory effect contain the previously mentioned *linear* (*ordinary*) and *nonlinear* (*null*) contributions.

The physical consequences of the memory effect described above are easy to visualize, but they do not constitute the best ways for detection. Due to the intrinsic weakness of GWs, the permanent change in the displacement and time delays in various detector dependent setup is also very small and cannot be directly measured with any currently known technology. The practically more relevant consequence of memory effect is the shifts and corrections to the GW waveforms, and it is the knowledge about the waveform correction that offers the best chance for a detection.

Earlier methods for computing the waveform of memory effect include the post-Newtonian (PN) approximation and various kinds of postprocessing techniques based on existing numerical waveforms [16,30,77–80]. We will follow [31] to calculate the memory waveforms in this paper.

Following [29,31], the Bondi-Sachs metric of a generic asymptotically flat spacetime containing GWs can be written as [17,18],

$$\begin{aligned} ds^2 = &-e^{2\beta}(Udu^2 + 2dudr) \\ &+ r^2\gamma_{AB}(d\theta^A - \mathcal{U}^A du)(d\theta^B - \mathcal{U}^B du), \end{aligned} \tag{1}$$

where $u = t - r$ is the retarded time, $\theta^A \in \{\theta^1, \theta^2\}$ are coordinates on the two-sphere, and U, β, $\mathcal{U}^A$ and γ_{AB} are functions of u, r, and θ^A. A special feature of the Bondi-Sachs metric is

$$g_{rr} = g_{rA} = 0. \tag{2}$$

The radial coordinate r is determined by requiring that the determinant of γ_{AB} is the same of that of the fixed round metric, denoted as q_{AB}, on the unit two-sphere,

$$\det(\gamma_{AB}) = \det(q_{AB}), \tag{3}$$

where, if written in the usual spherical coordinates,

$$q_{AB}d\theta^A d\theta^B = d\theta^2 + \sin^2\theta d\phi^2. \tag{4}$$

Note the metric q_{AB} will be used to raise and lower all capital Latin indices (e.g., A, B) throughout this paper.

The functions U, β, $\mathcal{U}^A$ and γ_{AB} in metric (1) can be determined by sourceless Einstein equations as

$$
\begin{aligned}
U &= 1-\frac{2m}{r}-\frac{2M}{r^2}+\mathcal{O}(r^{-3}),\\
\beta &= -\frac{C_2}{32r^2}-\frac{C_2^2}{48r^3}+\mathcal{O}(r^{-4}),\\
\gamma_{AB} &= q_{AB}+\frac{C_{AB}}{r}+\mathcal{O}(r^{-3}),\\
\mathcal{U}^A &= -\frac{D_B C^{AB}}{2r^2}+\frac{1}{r^3}\left[-\frac{2}{3}N^A+\frac{1}{16}D^A C_2\right.\\
&\quad\left.+\frac{1}{2}C^{AC}D^B C_{BC}\right]+\mathcal{O}(r^{-4}),
\end{aligned}
\tag{5}
$$

where all coefficient functions on the right-hand sides are functions of (u,θ^A) only, D^A is the covariant derivative associated with q_{AB}, and

$$
\begin{aligned}
&C_2 = C_{AB}C^{AB}, \qquad q^{AB}C_{AB}=0,\\
&\dot{m} = -\frac{1}{8}\dot{C}_{AB}\dot{C}^{AB}+\frac{1}{4}D_A D_B \dot{C}^{AB},\\
&\dot{N}_A = D_A m+\frac{1}{4}D_B D_A D_C C^{BC}-\frac{1}{4}D_B D^B D^C C_{CA}\\
&\quad+\frac{1}{4}D_B(\dot{C}^{BC}C_{CA})+\frac{1}{2}D_B\dot{C}^{BC}C_{CA},\\
&\dot{M} = -\frac{1}{2}D_A D^A\left(m+\frac{3}{8}C_{BC}\dot{C}^{BC}\right)+\frac{1}{3}D_A\dot{N}^A\\
&\quad-\frac{1}{4}(D_A\dot{C}_{BC})(D^A C^{BC}-2D^B C^{AC})\\
&\quad+\frac{1}{8}\dot{C}_{AB}\left(D_C D^C+\frac{3}{2}\right)C^{AB},
\end{aligned}
\tag{6}
$$

where C_{AB} is shear tensor, m is the Bondi mass aspect, M is the function of (u,θ^A) and N_A is Bondi angular-momentum aspect. Here an overdot means a derivative with respect to u. Follow [29,31,32], we rewrite N_A in terms of $\hat{N}_A$, $\hat{N}_A$ is

$$
\hat{N}_A = N_A - uD_A m-\frac{1}{16}D_A(C_{BC}C^{BC})-\frac{1}{4}C_{AB}D_C C^{BC}. \tag{7}
$$

The solution solves Einstein's equations to the $\mathcal{O}(r^{-3})$ order, i.e.,

$$
R_{\mu\nu}dx^\mu dx^\nu \le \mathcal{O}(r^{-4}), \tag{8}
$$

where $R_{\mu\nu}$ is the Ricci tensor of the Bondi-Sachs metric (1), $dx^\mu \in \{du, dr, d\theta^1, d\theta^2\}$, and we take

$$
du, dr \sim \mathcal{O}(r^0), \qquad d\theta^1, d\theta^2 \sim \mathcal{O}(r^{-1}). \tag{9}
$$

All dynamical properties of the solution are encoded in the two unconstrained functions of the shear C_{AB}.

Solutions with all possible values of C_{AB} form the solution space that preserves the structure of the Bondi-Sachs metric with the boundary conditions (2), (3), and (5). The solutions are related to each other through the BMS transformations,

$$
\begin{aligned}
\xi = f\partial_u &+ \left[Y^A-\frac{1}{r}D^A f+\frac{1}{2r^2}C^{AB}D_B f+\mathcal{O}(r^{-3})\right]\partial_A\\
&-\left[\frac{1}{2}rD_A Y^A-\frac{1}{2}D^A D_A f+\frac{1}{4r}(D_A C^{AB})D_B f\right.\\
&\left.+\frac{1}{4r}D_A(D_B f C^{AB})+\mathcal{O}(r^{-2})\right]\partial_r,
\end{aligned}
\tag{10}
$$

where

$$
f = \alpha(\theta^A)+\frac{1}{2}uD_B Y^B(\theta^A). \tag{11}
$$

Here $\alpha(\theta^A)$ is unconstrained and $Y^A(\theta^B)$ must obey the conformal Killing equation on the unit two-sphere,

$$
D_A Y_B + D_B Y_A = q_{AB}D_C Y^C. \tag{12}
$$

Under the action of (10), the shear transforms as

$$
\begin{aligned}
\delta C_{AB} &= f\dot{C}_{AB}-2D_A D_B f+q_{AB}D_C D^C f\\
&\quad+\frac{1}{2}(D_C Y^C)C_{AB}+\mathcal{L}_{\vec{Y}}C_{AB},
\end{aligned}
\tag{13}
$$

where $\mathcal{L}_{\vec{Y}}$ is the Lie derivative with $\vec{Y}=\{Y^1,Y^2\}$. Other functions in the solution will transform accordingly, and we refer to [29] for details on the transformation of the Bondi mass aspect m and the angular-momentum aspect N^A.

The BMS transformations (10) are examples of asymptotic symmetries which are associated with conserved charges that characterize different solutions in the solution space. In general, only the difference between the charges of a pair of solutions is defined (see [81] for a reader friendly exposition). In GW-free and matter-free cases, however, it is possible to write the charges for each solution directly,

$$
\begin{aligned}
Q = \frac{1}{16\pi}\int d^2\Omega &\left[4\alpha m-2u_0 Y^A D_A m+2Y^A N_A\right.\\
&\left.-\frac{1}{8}Y^A D_A C_2-\frac{1}{2}Y^A C_{AC}D_B C^{BC}\right],
\end{aligned}
\tag{14}
$$

where the integral is over a two-sphere near the null infinity and at the retarded time u_0.

In the usual spherical coordinates, the standard BMS algebra is generated by

$$
\begin{aligned}
\alpha &= t^0 - t^i n_i+\sum_{\ell=2}^{\infty}\sum_{m=-\ell}^{\ell}\alpha_{\ell m}Y_{\ell m},\\
Y^A &= w^{0i}e_i^A+w^{ij}e^A_{[i}n_{j]},
\end{aligned}
\tag{15}
$$

where $t^\mu = \{t^0, t^i\}$ and w^{0i}, w^{ij} are free parameters, $n_i = \{\sin\theta\cos\phi, \sin\theta\sin\phi, \cos\theta\}$, $e_i^A = D^A n_i$ and $Y_{\ell m}$ is the usual spherical harmonics. The corresponding charges are

$$Q = -P^\mu t_\mu + \frac{1}{2}J^{\mu\nu}w_{\mu\nu} + \frac{1}{4\pi}\sum_{\ell=2}^{\infty}\sum_{m=-\ell}^{\ell}\alpha_{\ell m}\mathcal{P}^*_{\ell m}. \quad (16)$$

Here P^μ is the usual four-momentum, $J^{\mu\nu}$ is the usual angular momentum, and $\mathcal{P}_{\ell m}$ are the *supermomenta* associated with the supertranslations, i.e., the $\ell \geq 2$ terms in α. So the standard BMS algebra is simply the Poincaré algebra extended with the supermomenta.

The BMS algebra can be extended if one allows for singular Killing vectors on the future null infinity [28,82]. To do this, it is more convenient to use the complex stereographic coordinates $(z, \bar{z})$ with $z = \cot(\theta/2)e^{i\phi}$ instead of the usual spherical coordinates. In this case, the conformal Killing equation requires $Y^z = Y^z(z)$ and $Y^{\bar{z}} = Y^{\bar{z}}(\bar{z})$, i.e., both to be meromorphic functions of their arguments. The corresponding Killing vector can be expanded with the set of vectors,

$$l_m = -z^{m+1}\partial_z, \qquad \bar{l}_m = -\bar{z}^{m+1}\partial_{\bar{z}}, \quad (17)$$

where $m \in \mathbb{Z}$. Among the vectors, $l_0, l_{\pm1}, \bar{l}_0$ and $\bar{l}_{\pm1}$ have already appeared in Eq. (15), while the rest are called the *superrotations*. Although the Killing vectors are singular for the superrotations, the corresponding charges have been shown to be finite [29]. The charges of the superrotations can be split to the spin parts, corresponding to operations analogs to the rotations in the Lorentz group, and the center-of-mass parts, corresponding to operations analogs to the Lorentz boost.

It has been realized that the displacement memory is related to changes in the supermomenta and the corresponding flux, the spin memory is related to changes in the spin parts of the super-angular momenta and the corresponding flux, and the center-of-mass memory effect is related to changes in the center-of-mass parts of the super-angular momenta and the corresponding flux [16,25–27]. As we have mentioned earlier, however, that for a true detection of the memory effect we have to focus on the waveforms. From this perspective, the displacement memory is characterized by a finite change in the GW strain, the spin memory is characterized by a change in the time integral of the magnetic part of the GW strain, while the center-of-mass memory effect is characterized by a change in the time integral of certain expression that has the dimension of the GW strain [16].

It was only recently that the displacement and spin memories are successfully captured in the SXS catalog [83,84] by using the Cauchy-characteristic extraction (CCE), in which one has to evolve a world tube produced by a Cauchy evolution to asymptotic infinity and then to extract the GW strain [85]. In [31], the authors use the BMS flux-balance law to calculate the memory effect from numerical waveforms known at the null infinity, and they find that the results agree with those from CCE well.

In the treatment of [31], the key quantity to calculate is the leading order spin-weight -2 GW strain,

$$h = \frac{1}{2}\bar{q}^A\bar{q}^B C_{AB} = \sum_{\ell\geq2}\sum_{|m|\leq\ell} h_{\ell m -2}Y_{\ell m}(\theta,\phi), \quad (18)$$

where q^A is the complex dyads [85], $q^A = -\{1, i\csc\theta\}$, ${}_{-2}Y_{\ell m}(\theta,\phi)$ is spin-weighted -2 spherical harmonics and the angles (θ,ϕ) are the inclination and the reference phase of the source respectively. In reverse, one has

$$C_{AB} = \frac{1}{2}(q_A q_B h + \bar{q}_A\bar{q}_B\bar{h}). \quad (19)$$

Splitting the shear into the electric and the magnetic components,

$$C_{AB} = \left(D_A D_B - \frac{1}{2}q_{AB}D_C D^C\right)\Phi + \epsilon_{C(A}D_{B)}D^C\Psi, \quad (20)$$

where ϵ_{AB} is the Levi-Civita tensor on the two-sphere, Φ and Ψ are the electric and magnetic parts of shear tensor C_{AB}. one has for the electric and magnetic memory effect, respectively,

$$\begin{aligned}\Delta J^{(E)} &= \frac{1}{2}\bar{q}^A\bar{q}^B\Delta C^{(E)}_{AB} = \frac{1}{2}\bar{\eth}^2\Delta\Phi \\ &= \frac{1}{2}\bar{\eth}^2\mathfrak{D}^{-1}\left[\Delta m + \frac{1}{4}\int_{-\infty}^{u}|\dot{h}|^2 du\right], \end{aligned} \quad (21)$$

$$\begin{aligned}\Delta J^{(B)} &= \frac{1}{2}\bar{q}^A\bar{q}^B\Delta C^{(B)}_{AB} = -\frac{1}{2}i\bar{\eth}^2\Delta\Psi \\ &= \frac{1}{2}i\bar{\eth}^2\mathfrak{D}^{-1}D^{-2}\mathrm{Im}\Big\{\bar{\eth}(\partial_u\hat{N}) \\ &\quad + \frac{1}{8}[\eth(3h\bar{\eth}\dot{\bar{h}} - 3\dot{h}\,\bar{\eth}\,\bar{h} + \dot{\bar{h}}\,\bar{\eth}\,h - \bar{h}\,\bar{\eth}\,\dot{h})]\Big\}. \end{aligned} \quad (22)$$

The $\Delta m = m(u) - m(-\infty)$ and $\hat{N} = q^A\hat{N}_A$. In Eqs. (21) and (22), Im means the imaginary part of the function, $D^2 = \bar{\eth}\eth$ is the usual Laplacian on the two-sphere, $\mathfrak{D} = \frac{1}{8}D^2(D^2+2)$, and $\eth$ and $\bar{\eth}$ are the spin-weight operators in the Newman-Penrose convention [86],

$$\begin{aligned}\eth_s Y_{\ell m} &= +\sqrt{(\ell-s)(\ell+s+1)}\,{}_{s+1}Y_{\ell m}, \\ \bar{\eth}_s Y_{\ell m} &= -\sqrt{(\ell+s)(\ell-s+1)}\,{}_{s-1}Y_{\ell m}. \end{aligned} \quad (23)$$

For the spin weight 0 spherical harmonics $Y_{\ell m}$,

$$D^2 Y_{\ell m} = -\ell(\ell+1) Y_{\ell m},$$
$$\mathfrak{D} Y_{\ell m} = \frac{1}{8}(\ell+2)(\ell+1)\ell(\ell-1) Y_{\ell m}. \quad (24)$$

The $\ell \leq 1$ modes of $Y_{\ell m}$ are in the kernel of $\mathfrak{D}$, so $\mathfrak{D}^{-1}$ is defined by projecting out the $\ell \leq 1$ modes [31],

$$\mathfrak{D}^{-1} Y_{\ell m} = \begin{cases} 0: & \ell \leq 1, \\ [\frac{1}{8}(\ell+2)(\ell+1)\ell(\ell-1)]^{-1} Y_{\ell m}: & \ell \geq 2. \end{cases} \quad (25)$$

The first term in the right-hand side of Eq. (21) is the ordinary part of the displacement memory, and the second term is the null part. The Bondi mass aspect m can be written in terms of Weyl scalar Ψ_2 and h as

$$m = -\mathrm{Re}\left[\Psi_2 + \frac{1}{4}\dot{h}\,\bar{h}\right]. \quad (26)$$

Similarly, the first term in the right-hand side of Eq. (22) is the ordinary part of spin memory mode and the second part is the null part. $\hat{N}$ can be written in terms of Weyl scalar Ψ_1 and h as

$$\hat{N} = 2\Psi_1 - u\eth m - \frac{1}{8}\eth(h\bar{h}) - \frac{1}{4}\bar{h}\eth h. \quad (27)$$

As discussed in [31], $\Delta J^{(E)}$ is dominated by the displacement memory, $\int \Delta J^{(B)}(u)du$ is the spin memory, while the explicit formula for computing the center-of-mass memory by using the BMS flux-balance law is not known yet. The detection of the center-of-mass memory effect using PN waveform has been studied in [16]. It has been found that, for a future ground-based detector such as the Einstein Telescope, which can achieve a signal-to-noise ratio (SNR) at the order $\mathcal{O}(10^3)$ for a signal like GW150914, can only detect the ordinary part of the center-of-mass memory effect with a SNR several orders of magnitude below unit. The prospect for space-based detector will be similar, so the chance for detection is negligible for TianQin. Therefore, in this work, we only consider the displacement memory and the spin memory mode.

III. WAVEFORM MODEL

We use the IMRPhenomXHM waveform [87–89] to calculate the displacement memory strain with Eq. (21) and the spin memory strain with Eq. (22),

$$h_{\mathrm{dis}} = \Delta J^{(E)}, \qquad h_{\mathrm{spin}} = \Delta J^{(B)}. \quad (28)$$

IMRPhenomXHM can fastly produce relatively accurate waveforms containing the most dominant modes, such as (2, 2), (2,1), (3,3), (3,2), and (4,4), which are expected to contribute to the memory effect. It should also be noticed that IMRPhenomXHM is an aligned-spin model and has only been calibrated with NR for mass ratios $q = m_1/m_2 \in [1, 18]$, but it has been noted in [87] that the waveforms still have reasonable accuracy outside of the calibration region. So we will use waveforms with mass ratios in the region $q \in [1, 23]$ in this work.

In our calculations, we use IMRPhenomXHM to generate the frequency domain waveform first, and then use the inverse Fourier transform method from LALSimulation [90] to generate the time domain waveform, which is necessary for calculating the memory effect. We only keep dominant modes for the displacement memory and the spin memory mode, i.e., $h_{(2,0)}$ and $h_{(3,0)}$, respectively. This is reasonable, since the higher ℓ modes are strongly suppressed, as one can see from Eq. (25).

To assess the detection potential of memory effects, we need to convert waveforms to the frequency domain by a Fourier transformation. We use Planck-taper window [91] to window the time-domain waveform to remove edge effects. In the calculation, we choose $\epsilon = 0.04$ (see Eq. (7) in McKechan *et al.* [91] for the detail of window function).

Since the memory effect is always subdominant compared to the full GW strain, one should search for memory effect in GW signals with the highest possible SNR. So we focus on MBHBs with masses in the range $10^4\ \mathrm{M}_\odot \sim 10^7\ \mathrm{M}_\odot$ in this study. In the following part of this work, all the mass mentioned are redshifted mass.

It is important to determine how much data will be needed in the calculate the memory effect. For this we note that the vast majority of the SNRs produced by MBHBs on TianQin can be obtained within the last hour of data before merger [75,76]. But as we will see below, we will not need a full hour of data for total masses near $10^4\ \mathrm{M}_\odot$. We also note the memory effect is mainly accumulated during the merger phase when the most energy and angular momentum are radiated away, while the spin memory may get relatively more contribution from the inspiral phase [30,31]. So we choose to calculate the memory effect by keeping a fixed number of waveform cycles (for any given mass ratio) before merger, where the number of cycles is defined as [92]

$$\mathcal{N} = \frac{1}{32\pi^{8/3}}\left(\frac{GM_c}{c^3}\right)^{-5/3}(f_{\mathrm{min}}^{-5/3} - f_{\mathrm{max}}^{-5/3}). \quad (29)$$

Here f_{min} and f_{max} are the frequencies at the beginning and the end points of the waveform, G is gravitational constant, c is light speed, M_c is the chirp mass,

$$M_c = \frac{(m_1 m_2)^{3/5}}{(m_1+m_2)^{1/5}}. \quad (30)$$

For the efficiency of calculation, we have generated the waveforms for a chosen total mass $(2 \times 10^6\ \mathrm{M}_\odot)$

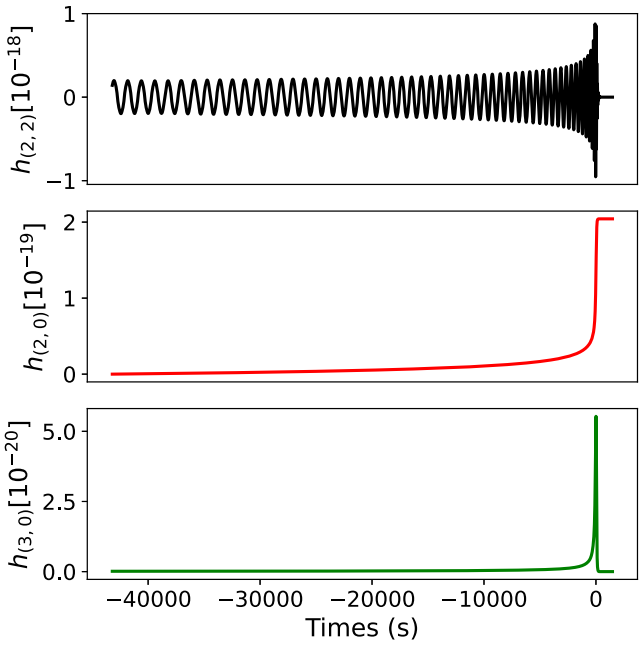

FIG. 1. Example of waveforms generated with IMRPhenomXHM. Plotted with a nonspinning MBHB with mass ratio $q = 1$, total mass $M = 10^6\ \mathrm{M}_\odot$ at luminosity distance $D_\mathrm{L} = 2$ Gpc. The top panel is the real part of dominant GW mode $h_{(2,2)}$, the middle panel is the real part of dominant mode of displacement memory $h_{(2,0)}$, and the bottom panel is the imaginary part of dominant spin memory mode $h_{(3,0)}$. The cycles of the waveform for this plot is about 57.

with a given duration (one day) at different symmetric mass ratios,

$$\eta = \frac{m_1 m_2}{(m_1 + m_2)^2}, \tag{31}$$

ranging from $\eta = 0.04$ to $\eta = 0.25$ at a 0.01 incremental rate, and the waveform is then used for all source masses through appropriate scaling (For sources with total mass $10^4\ \mathrm{M}_\odot$ and $10^7\ \mathrm{M}_\odot$, this corresponds to a duration of 0.12 hour and 5 day, respectively). The number of cycles involved in such waveforms increases monotonically when the symmetric mass ratio is lowered, varying from about 57 for $\eta = 0.25$ to about 113 for $\eta = 0.04$. The lost SNR for cycles not included is expected to be negligible. We have explicitly checked that the difference between the memory SNRs from waveforms keeping the last 150 cycles and the last 50 cycles before merger is no greater than 0.026%, for equal mass sources with different total masses. For unequal-mass sources, the number of cycles in the waveform is always greater than that of the equal-mass sources and so the lost SNR is expected to be even smaller. In Fig. 1, we give an example of the waveforms generated with IMRPhenomXHM. One can see that the accumulation of memory effect is most significant near the time of merger.

IV. DETECTION POTENTIAL

In this section, we study the prospect of using TianQin to detect the memory effect.

The data stream output from a detector can be schematically written as

$$d(t) = s(t) + n(t), \tag{32}$$

where $s(t)$ is the GW signal registered by the detector and $n(t)$ is the noise in the data stream.

The registered signal depends on the detector through the antenna pattern functions. For space-based GW detectors like TianQin and LISA, they are given by

$$\begin{aligned} F_+(\theta,\phi,\psi) &= \frac{\sqrt{3}}{2}\left[\frac{1}{2}(1+\cos^2\theta)\cos 2\phi\cos 2\psi \right. \\ &\quad \left. - \cos\theta \sin 2\phi \sin 2\psi\right], \\ F_\times(\theta,\phi,\psi) &= \frac{\sqrt{3}}{2}\left[\frac{1}{2}(1+\cos^2\theta)\cos 2\phi\sin 2\psi \right. \\ &\quad \left. + \cos\theta \sin 2\phi \cos 2\psi\right], \end{aligned} \tag{33}$$

where the θ and ϕ are the position of the source in the detector frame, and ψ is the polarization angle. For any incoming GW signal with the usual plus and cross modes, $h(t,\iota,\varphi_c) = h_+(t,\iota,\varphi_c) - ih_\times(t,\iota,\varphi_c)$, where ι and φ_c are the inclination and the reference phase, respectively, the registered signal is given by

$$s(t) = F_+(\theta,\phi,\psi)h_+(t,\iota,\varphi_c) + F_\times(\theta,\phi,\psi)h_\times(t,\iota,\varphi_c). \tag{34}$$

For a preliminary estimation, we focus on the sky-averaged response of GWs,

$$\langle s^*(t)s(t)\rangle = \int_0^{+\infty} S_h(f)\bar{R}(f)df, \tag{35}$$

where $S_h(f)$ is the power spectral density (PSD) of the incoming GW signal and $\bar{R}(f)$ is the sky-averaged response of the detector. In this work, we use

$$\begin{aligned} S_h(f) &= \frac{2}{T}|\tilde{h}_{+,\times}(f)|^2 \equiv \frac{2}{T}|\tilde{h}(f)|^2, \\ \bar{R}(f) &= \frac{3}{10}\left[1 + \left(\frac{2fL_0}{0.41}\right)^2\right]^{-1}, \end{aligned} \tag{36}$$

where T is the time span of the data stream, $\tilde{h}_{+,\times}(f)$ are the Fourier components of $h_{+,\times}(t)$, and L_0 is the arm-length of the detector.

The noise $n(t)$ is usually given in terms of its PSD,

$$S_N(f) = \frac{2}{T}|\tilde{n}(f)|^2, \tag{37}$$

where $\tilde{n}(f)$ is the Fourier component of $n(t)$. For a space-based detector like TianQin and LISA, the noise can be grossly grouped into two categories: those from the propagation of the laser used to measure the change of spacetime due to the passage of GWs and those from the irregular motion of the test masses serving as reflecting endpoints for the lasers. The former is quantified with the total displacement measurement noise in a single laser link, denoted by S_x, and the latter is quantified with the residue acceleration noise of a test mass in the sensitive direction, denoted by S_a. The structure of $S_N(f)$ and the constants L_0, S_x and S_a are different for different detectors. For TianQin, $L_0 = \sqrt{3} \times 10^8$ m, and the following noise model is used in the process of mission development [61,62],

$$\begin{aligned} S_N(f) &= \frac{1}{L_0^2}\left[S_x + \frac{4S_a}{(2\pi f)^4}\left(1 + \frac{10^{-4}\ \text{Hz}}{f}\right)\right], \\ S_x^{1/2} &= 1 \times 10^{-12}\ \text{m/Hz}^{1/2}, \\ S_a^{1/2} &= 1 \times 10^{-15}\ \text{m/s}^2/\text{Hz}^{1/2}. \end{aligned} \tag{38}$$

The huge number of Galactic compact binaries, most of which are ultracompact double white dwarf systems, can generate a foreground confusion noise that may affect the detection of GWs from other sources. However, it has been shown that the expected foreground confusion noise for the TianQin is relatively weak [67]. So we will not consider it in this work. For LISA, the parameters of the Galactic confusion noise [93,94] are for four years of data.

The sky averaged sensitivity, or equivalently the amplitude spectral density (ASD), of TianQin is define as

$$h_{\text{eff}}(f) = \sqrt{S_n(f)}, \qquad S_n(f) \equiv \frac{S_N(f)}{\bar{R}(f)}. \tag{39}$$

The numerical results are plotted in Fig. 2. As a comparison, we plot the sensitivity curve of LISA [94], for which the contribution of the foreground confusion noise is non-negligible. We also plot the strains for the dominant mode $h_{(2,2)}$, the dominant mode of displacement memory $h_{(2,0)}$, and the dominant spin memory mode $h_{(3,0)}$.

A. SNR

The SNR is a key quantity one can use to assess the detection potentia of a signal, which is defined as

$$\rho = \sqrt{4\int_{f_{\min}}^{f_{\max}} \frac{|\tilde{h}(f)|^2 \bar{R}(f)}{S_N(f)} df}, \tag{40}$$

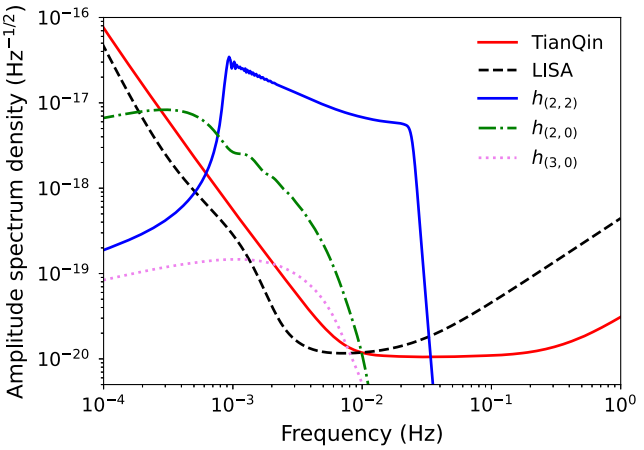

FIG. 2. The sensitivity curves of TianQin and LISA, together with the dominant modes, $h_{(2,2)}$, $h_{(2,0)}$, and $h_{(3,0)}$, for the usual GW strain, the displacement memory and the spin memory mode, respectively, plotted with a nonspinning MBHB with mass ratio $q = 1$, total mass $M = 10^6\ \text{M}_\odot$, inclination $\iota = \pi/4$ and luminosity distance $D_{\text{L}} = 2$ Gpc.

where $f_{\min}$, $f_{\max}$ are the minimal and maximal frequency limits of the waveform. For ground-based detectors, one may use an SNR threshold as low as $\rho = 3$ to claim a detection of the memory effect [48,95,96]. However, for space-based detectors, there could be several signals coexisting in the data, potentially making it more difficult to identify the memory effect. But since the actual SNR threshold is still not well studied so far, we will use the set of thresholds $\rho = 3$, 5, 8 to get an indicative result for the detection potential of TianQin. As an explicit example, for the source parameters used in Fig. 2, the SNRs are: $\rho_{(2,2)} = 1112.2$, $\rho_{(2,0)} = 14.7$, and $\rho_{(3,0)} = 3.8$.

There are several parameters that can strongly affect the SNR. The most significant one is the inclination angle ι, and the dependence of inclination has been well studied (see, e.g., [55,78,80]). We plot the SNR of memory effects as a function of ι in Fig. 3. For the displacement memory, the SNR will get its maximum at $\iota = \pi/2$, and approaches to 0 as ι approaches to 0 and π. On the other hand, for the spin memory mode, the SNR will be 0 while $\iota = \pi/2$, and get its maximum near $\iota = 3\pi/10$ and $\iota = 7\pi/10$. For all the examples to be studied in the following part, we will choose $\iota = \pi/2$ for the displacement memory and $\iota = \pi/4$ for the spin memory mode.

Another important parameter is the spin of the components of the binaries, which can increase the efficiency of energy loss through GW radiation [97,98]. In our situation, we consider the aligned spin systems. We use the effective spin defined by [99,100],

$$\chi = \frac{m_1\chi_{s_1} + m_2\chi_{s_2}}{m_1 + m_1}, \tag{41}$$

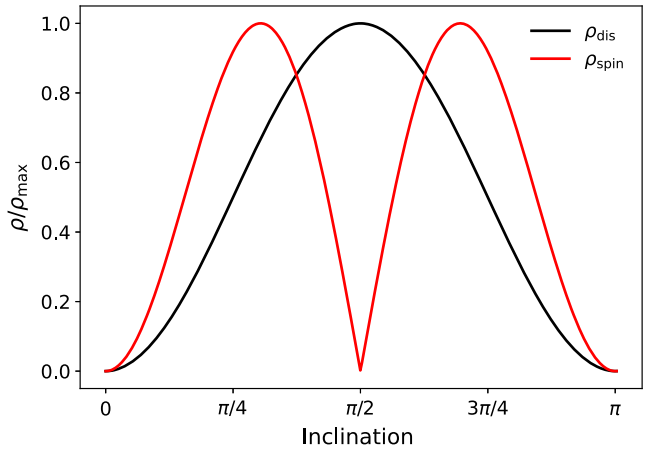

FIG. 3. Dependence of SNR on the inclination angle ι. Note different values of ρ_{max} are used for the displacement memory and the spin memory mode. Plotted using a MBHB with mass ratio $q = 1$, total mass $M = 10^6$ $M_\odot$ and luminosity distance $D_L = 2$ Gpc.

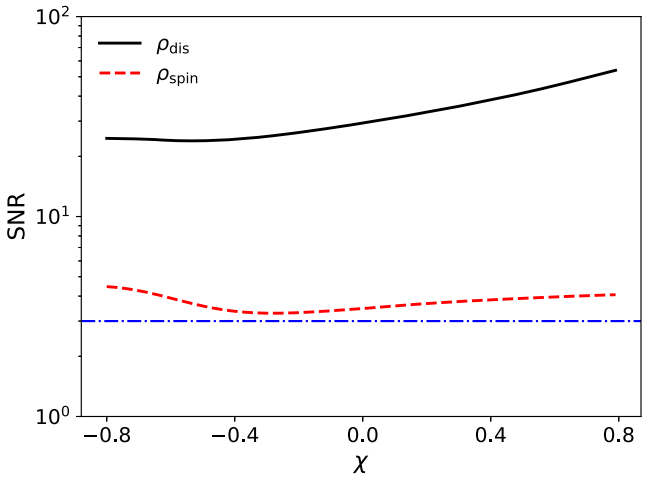

FIG. 4. Dependence of SNR on the effective spin χ. Plotted using a MBHB with mass ratio $q = 1$, total mass $M = 10^6$ $M_\odot$ and luminosity distance $D_L = 2$ Gpc. The blue horizontal line represents SNR equal to 3. We choose inclination $\iota = \pi/2$ for displacement memory, and inclination $\iota = \pi/4$ for spin memory mode.

where χ_{s_1,s_2} is aligned dimensionless spin components of two black holes and are defined as

$$\chi_{s_1,s_2} = \frac{\vec{S}_{1,2} \cdot \vec{L}}{m_{1,2}^2 |\vec{L}|}, \tag{42}$$

where $\vec{S}_{1,2}$ are the spins (intrinsic angular momentum) of the two individual black holes, $\vec{L}$ is the orbital angular momentum and $m_{1,2}$ are the masses of two black holes. The dependence of SNR on the effective spin χ is plotted in Fig. 4. One can see that the SNR of the displacement memory increases nearly monotonically with χ, while the SNR of the spin memory mode does not vary too much with χ.

It is expected that the SNR will strongly depend on the source distance, for it is inversely proportional to the magnitude of the GW strain. In Fig. 5, we plot the horizon distance for detection in terms of the redshift z as a function of the total mass M. For the displacement memory, the maximum redshifts for SNRs equal to 3, 5, 8 are $z = 4.6$, $z = 2.98$ and $z = 2.03$, respectively. For the spin memory mode, the maximum redshifts for SNR equal to 3 is $z = 0.48$. As a comparison, we also give the results on LISA and the joint detection with TianQin and LISA (denoted as TianQin + LISA). The horizon distance for LISA is almost twice of that for TianQin within a large part of the mass ranges, with the maximum redshifts reaching $z = 10.3$, $z = 6.6$, $z = 4.4$ for the SNRs of the displacement memory equal to 3, 5, and 8, and the maximum redshift for detecting the spin memory mode with SNR equal to 3 is $z = 1.7$. There is also obvious improvement of TianQin + LISA over LISA alone, with the contribution of TianQin being more significant near the lower mass end.

The dependence of SNR on the total mass M and the symmetric mass ratio η is plotted in Fig. 6 for different values of χ. The maximal SNRs for both displacement memory and spin memory mode appear around $\eta = 0.25$, which is consistent with the expectation that systems of equal mass can radiate the most energy and angular momentum during GW radiation and thus can incur the largest memory effect. For the displacement memory, it is possible to have SNRs passing $\rho = 3$ for η roughly in the range 0.06–0.25, while for the spin memory mode, the allowed range for η is narrowed to the small region of roughly 0.22–0.25. Depending of the values of the χ, the maximal SNRs for the displacement memory appear roughly in the range 4×10^5 $M_\odot$–8×10^5 $M_\odot$, while the maximal SNRs for the spin memory mode appear roughly in

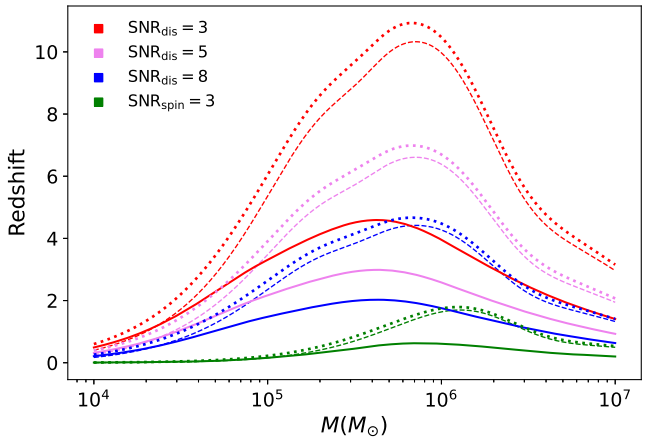

FIG. 5. The dependence of detection horizon for memory effect on the total mass, at SNRs equal to 3, 5, 8 for the displacement memory and the SNR equal to 3 for the spin memory mode. Other source parameters are $q = 1$ and $\chi = 0.8$. Three detector configurations are considered: TianQin (solid), LISA (dashed), and TianQin + LISA (dotted).

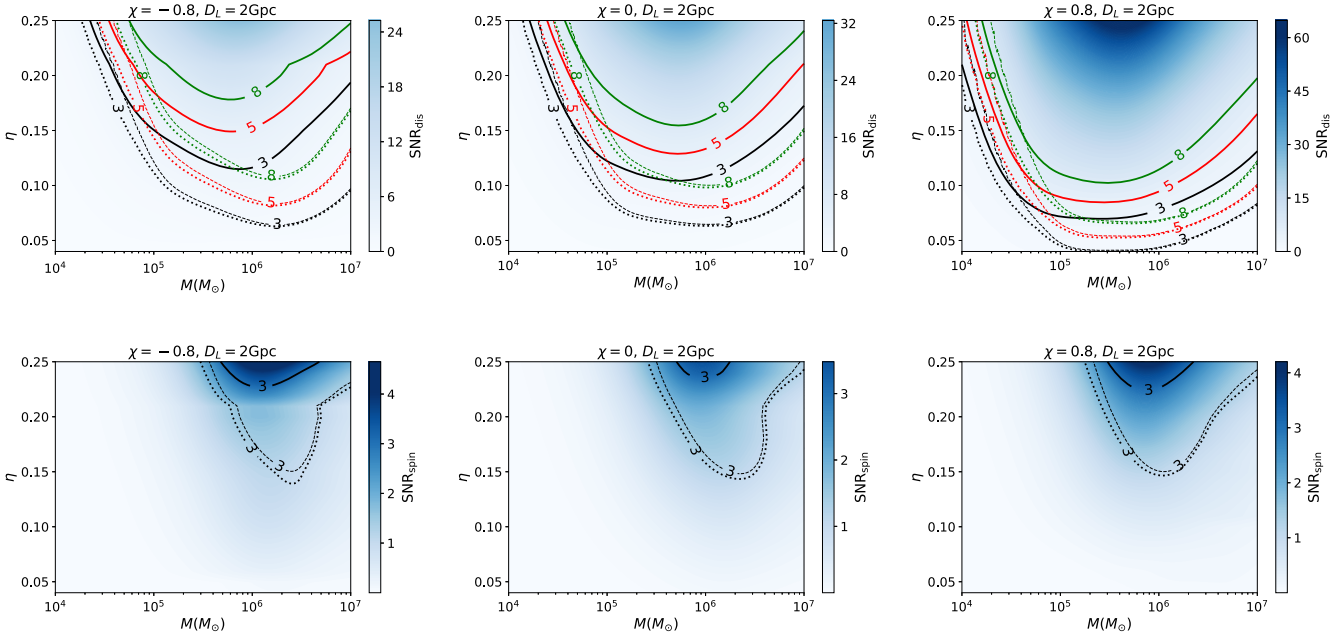

FIG. 6. The dependence of SNRs on the symmetric mass ratio η and the total mass M, for three values of the effective spin, $\chi = -0.8$, 0, 0.8, and fixed luminosity distance $D_{\rm L} = 2$ Gpc. The upper panel is for the displacement memory and the lower panel is for the spin memory mode. The numbers on the contours are the corresponding SNRs. Three detector configurations are considered: TianQin (solid), LISA (dashed), and TianQin + LISA (dotted).

the range 8×10^5 $M_\odot$–1.5×10^6 $M_\odot$. As a comparison, we have also included the contours for LISA and TianQin + LISA in the same plots. One can see that in detecting the displacement memory, LISA is superior in most parameter space, while TianQin can be competitive in a small region near the lower mass end and such advantage grows bigger with χ. There is obvious improvement of TianQin + LISA over LISA at the lower mass end of the plots. In the detection of the spin memory mode, LISA is always superior than TianQin while the improvement of TianQin + LISA is obvious for all mass ranges.

B. Detection number

It is known that TianQin can detect several to dozens of MBHBs per year [75]. So a natural question to ask is how many of the detected events will contain memory effect that is directly detectable.

There is still a lot of uncertainty in the astrophysical models that determine the population of MBHBs in the universe. In this work, we use three different models for merger history of massive black holes which have been used in [75]. These three models are generated using the semi-analytic model proposed in [101] and successively improved in [102,103]. One model is referred as "popIII" which corresponds to a light seed model [104], and the other two models are referred as "Q3_d" and "Q3_nod," which correspond to two heavy seed models [105–107] with and without the time delay between the merger of a MBHB and that of their host galaxies.

In [75], 1000 mock catalogs have been generated for each of the astrophysical models. We search in each of these mock catalogs for events containing memory effect with SNRs exceeding $\rho = 3$, counting the detection number, and then average over the 1000 mock catalog for each of the astrophysical models.

The result is given in Table I. One can see that, depending on the astrophysical models used, TianQin can in average detect 0.5–2.0 events whose displacement memory has SNRs no less than 3 and about 0.1–0.7 events whose displacement memory has SNRs no less than 8. On the one hand, these result suggests that the chance for TianQin to directly detect the displacement memory is not very high. But on the other hand, these results suggest that the chance for TianQin to directly detect the displacement memory is not fully negligible. In contrast, less than 0.2 events are expected to be detected which will contain the spin memory mode whose SNR can reach 3, meaning that the chance for TianQin to directly detect the spin memory mode from a single MBHB event is likely negligible. The results on LISA have also been included in Table I. One can see that the expected detection number of LISA is about 2–4 times that of TianQin, depending on which astrophysical model and which SNR value one is looking at.

V. RELEVANT PARAMETER SPACE

Due to the important application of MBHB events in fundamental physics [69,70], astrophysics [75] and cosmology [108], each detected MBHB event would be extremely precious and it is extremely important to have accurate

TABLE I. The expected IMR detection number and both displacement memory and spin memory mode detection number on TianQin and LISA detectors for "popIII," "Q3_d," and "Q3_nod" astrophysical models.

	IMR	$\mathcal{M}$ > Threshold	$\rho_{\rm dis} > 3$	$\rho_{\rm dis} > 5$	$\rho_{\rm dis} > 8$	$\rho_{\rm spin} > 3$	$\rho_{\rm spin} > 5$	$\rho_{\rm spin} > 8$
popIII TianQin	56.8	0.9	0.5	0.3	0.1	~ 0	~ 0	~ 0
Q3_d TianQin	18.1	0.9	0.6	0.3	0.2	~ 0	~ 0	~ 0
Q3_nod TianQin	271.4	3.6	2.0	1.2	0.7	0.2	0.1	~ 0
popIII LISA	148.35	3.3	1.6	0.7	0.4	0.1	~ 0	~ 0
Q3_d LISA	37.4	4.9	2.6	1.4	0.8	0.2	0.1	~ 0
Q3_nod LISA	295.5	12.2	5.8	2.6	1.4	0.4	0.2	0.1

waveform models to precisely measure the source parameters. As we have mentioned before, although the memory effect is physically interesting on its own right, it can also lead to systematic errors if not properly taken into consideration in waveform modeling. In this section, we study when the contribution of memory effect will become non-negligible. One can intuitively reason that this should be equivalent to when the memory effect will become detectable. So our key task here is to determine the relevant parameter space.

The effect of neglecting the memory effect in the waveforms can be quantified using the mismatch between the waveforms with and without the memory effect. For two different waveform models $\tilde{h}_1(f)$ and $\tilde{h}_2(f)$, the mismatch is defined as

$$\mathcal{M} = 1 - \frac{\langle \tilde{h}_1, \tilde{h}_2 \rangle}{\sqrt{\langle \tilde{h}_1, \tilde{h}_1 \rangle \langle \tilde{h}_2, \tilde{h}_2 \rangle}}, \tag{43}$$

where

$$\langle \tilde{h}_1, \tilde{h}_2 \rangle = 4\mathrm{Re} \int_{f_{\rm min}}^{f_{\rm max}} \frac{\tilde{h}_1(f)\tilde{h}_2^*(f)}{S_n(f)} df. \tag{44}$$

The systematic errors introduced by a reliable waveform need to be lower than statistical errors. In high SNR regime, the statistical errors can be estimated from the inverse of Fisher matrix $\Gamma_{ij} = (\partial_i h | \partial_j h)$ (where i, j are the waveform's parameters), and these errors are decreased as SNR^{-1} [109]. The threshold value of mismatch is given by [110–112]

$$\mathcal{M}_{th} = \frac{D}{2\rho^2}, \tag{45}$$

where D is the number of parameters whose estimation is affected by the waveform model accuracy. In our case, we have $D = 4$. One needs $\mathcal{M} < \mathcal{M}_{th}$ to ensure that the

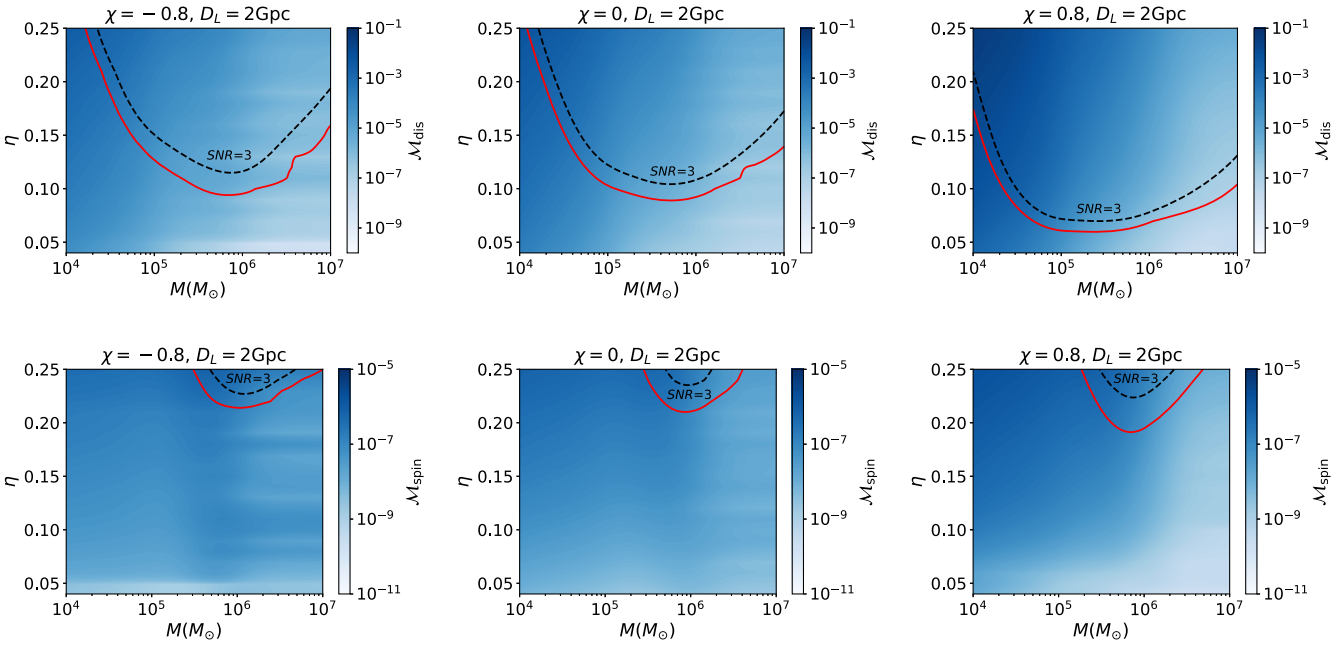

FIG. 7. The dependence of mismatch on the symmetric mass ratio η and the total mass M, for three values of the effective spin, $\chi = -0.8, 0, 0.8$, and fixed luminosity distance $D_{\rm L} = 2$ Gpc. The upper panel is for the displacement memory while the lower panel is for the spin memory mode. The black dashed lines mark where the memory SNR equals 3. The red solid lines mark where the mismatch reaches the threshold determined by Eq. (45), in which ρ is calculated using the complete waveform but containing no memory effect.

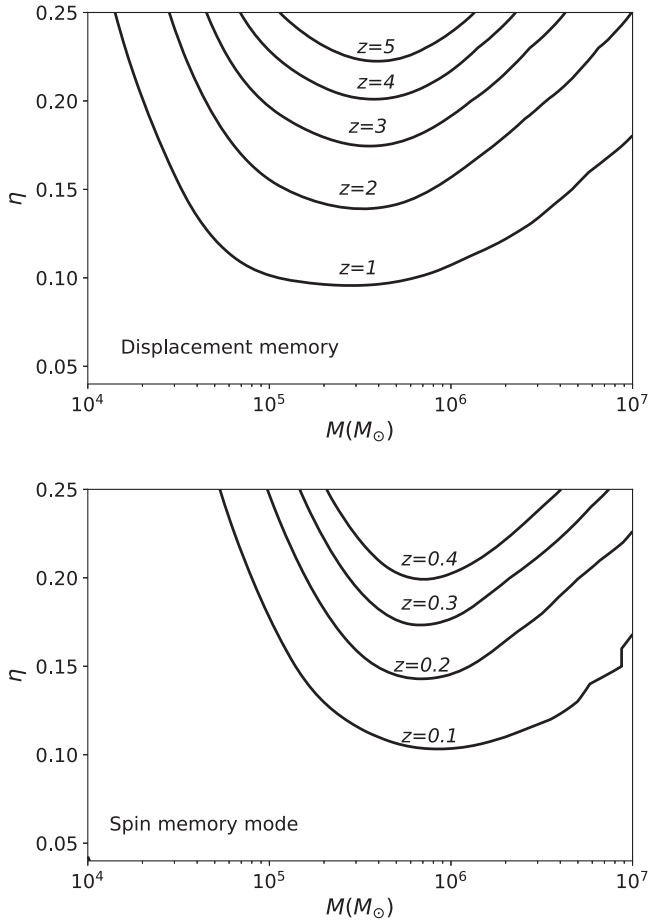

FIG. 8. The critical contour of mismatch at different redshift values. We have used $\chi = 0.8$ in the plots.

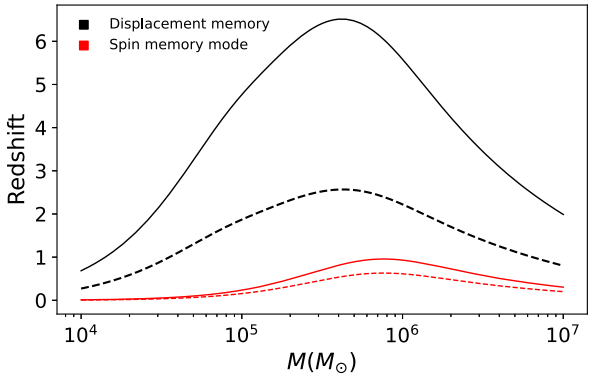

FIG. 9. The horizon distance in redshift for the detection with a criterion of mismatch and SNR in terms of reshifted total mass. The calculation is made by the MBHB with $M = 10^6$ M$_\odot$, $q = 1$ and $\chi = 0.8$. In calculation, we choose inclination $\iota = \pi/2$ for displacement memory, and inclination $\iota = \pi/4$ for spin memory mode.

parameter estimation is unbiased. It should be noted that the results given by Eq. (45) become unreliable as the SNR decreases [109,112].

The dependence of the mismatch on the symmetric mass ratio η and the total mass M, for several values of the effective spin χ and the fixed luminosity distance $D_{\rm L}$, is plotted in Fig. 7. One can see the contours for the mismatch threshold and those for the SNR equal to 3 are close to each other.

We also plot the critical contours where the mismatch reaches its threshold for different redshift values on M-η plane in Fig. 8. One can see that the critical contours shrink when the redshift is increased. For a source with total mass near 4×10^5 M$_\odot$, one should consider the contribution of displacement memory to the waveform even when the source is beyond redshift 5, while for the spin memory mode, it can only have influence for very small redshift, another indication that spin memory is unlikely to be directly detected with a single source.

In Fig. 9, we compare the horizon distance deduced by using the mismatch threshold and by requiring $\rho = 3$. One can see that the horizon distance to pass the threshold of mismatch is always larger than requiring $\rho = 3$. Using the criterion of mismatch, the maximum redshift is $z = 6.37$ for the displacement memory and $z = 0.58$ for the spin memory mode.

VI. CONCLUSION

Among all the curious effects, the radiation of GWs also cause permanent changes in the background spacetime. Such changes are caused not only by the changes in the BMS charges in spacetime, but also by the energy and angular momentum fluxes that go to the null infinity. So the detection of memory effect will serve as an important portal to study the nature of gravity and spacetimes.

These permanent changes, which are called the displacement, spin and center-of-mass memory, are related to the various types of BMS transformations and their extensions. Such connection has enabled the calculation of the displacement memory strain and the spin memory mode strain using the BMS flux-balance laws.

In this paper, we study the prospect of using TianQin, a planned space-based GW detector, to directly detect the memory effect.

The SNRs depend strongly on many of the source parameters. For the displacement memory, the maximal SNRs can be achieved with the inclination angle $\iota = \pi/2$, large effective spin, nearly equal mass and with total masses in the range 4×10^5 M$_\odot \sim 8 \times 10^5$ M$_\odot$. For the spin memory mode, the maximal SNRs can be achieved with the inclination angle near $\iota = 3\pi/10$ and $\iota = 7\pi/10$, nearly equal mass and with total masses in the range 8×10^5 M$_\odot \sim 1.5 \times 10^6$ M$_\odot$. With favorable source parameters, the memory SNRs can reach 3 for sources located as far as $z \approx 4.6$ for detecting the displacement memory and $z \approx 0.48$ for detecting the spin memory mode. By using currently available astrophysical models for MBHBs, For

memory effect with a SNR equal to 3, we find that TianQin can detect about 0.5–2.0 MBHB events with the displacement memory effect, and less than 0.7 events with spin memory mode during its 5 years observation. Thus TianQin will have a low but non-negligible chance to detect the displacement memory while the chance to detect the spin memory from a single MBHB event is likely negligible.

We also study the question of when the contribution of memory effect will become non-negligible in the waveform modeling of MBHBs. We find that contour of SNR $= 3$ are included in the criterion for the mismatch beyond the threshold. By using (nearly) optimal values for the inclination angle and the effective spin, we determine the parameter space in which the memory effect can be safely neglected.

We note LISA can do better than TianQin in detecting the memory effect for most sources while TianQin can become competitive for sources with lower total masses. With the current astrophysical models on MBHBs, the expected detection number of LISA is about 2–4 times that of TianQin, depending on which astrophysical model and which SNR value one is looking at. We also note TianQin + LISA can have obvious improvement over each of the individual detectors.

ACKNOWLEDGMENTS

We are grateful to Keefe Mitman, Michael Boyle, Moritz Hübner, Oliver Boersma, Alberto Mangiagli and Neev Khera for their kind helps. We thank Yiming Hu, Qingfei Zhang and Han Wang for many useful discussions. We thank Alberto Sesana and Enrico Barausse for sharing their simulated catalog of massive black holes. We also thank the anonymous referee for his valuable comments, which helped to improve the manuscript. We acknowledge the usage of the calculation utilities of LALSuite [90], SXS [84], NumPy [113], and SciPy [114], and plotting utilities of MATPLOTLIB [115]. This work has been supported by Guangdong Major Project of Basic and Applied Basic Research (Grant No. 2019B030302001).

[1] B. P. Abbott *et al.* (LIGO Scientific, Virgo Collaborations), Phys. Rev. X **9**, 031040 (2019).
[2] R. Abbott *et al.* (LIGO Scientific, Virgo Collaborations), Phys. Rev. X **11**, 021053 (2021).
[3] R. Abbott *et al.* (LIGO Scientific, Virgo, KAGRA Collaborations), arXiv:2111.03606.
[4] B. P. Abbott *et al.* (LIGO Scientific, Virgo Collaborations), Astrophys. J. Lett. **882**, L24 (2019).
[5] R. Abbott *et al.* (LIGO Scientific, Virgo Collaborations), Astrophys. J. Lett. **913**, L7 (2021).
[6] R. Abbott *et al.* (LIGO Scientific, Virgo, KAGRA Collaborations), arXiv:2111.03634.
[7] B. P. Abbott *et al.* (LIGO Scientific, Virgo Collaborations), Phys. Rev. D **100**, 104036 (2019).
[8] R. Abbott *et al.* (LIGO Scientific, Virgo Collaborations), Phys. Rev. D **103**, 122002 (2021).
[9] R. Abbott *et al.* (LIGO Scientific, Virgo, KAGRA Collaborations), arXiv:2112.06861.
[10] L. Blanchet and T. Damour, Phys. Rev. D **46**, 4304 (1992).
[11] L. Blanchet, Living Rev. Relativity **17**, 2 (2014).
[12] Y. B. Zel'dovich and A. G. Polnarev, Sov. Astron. **18**, 17 (1974).
[13] V. B. Braginsky and K. S. Throne, Nature (London) **327**, 123 (1987).
[14] D. Christodoulou, Phys. Rev. Lett. **67**, 1486 (1991).
[15] L. Bieri and D. Garfinkle, Phys. Rev. D **89**, 084039 (2014).
[16] D. A. Nichols, Phys. Rev. D **98**, 064032 (2018).
[17] H. Bondi, M. G. J. van der Burg, and A. W. K. Metzner, Proc. R. Soc. A **269**, 21 (1962).
[18] R. K. Sachs, Proc. R. Soc. A **270**, 103 (1962).
[19] J. de Boer and S. N. Solodukhin, Nucl. Phys. **B665**, 545 (2003).
[20] G. Barnich and C. Troessaert, Phys. Rev. Lett. **105**, 111103 (2010).
[21] G. Barnich and C. Troessaert, Proc. Sci. CNCFG2010 (**2010**) 010.
[22] D. Kapec, V. Lysov, S. Pasterski, and A. Strominger, J. High Energy Phys. 08 (2014) 058.
[23] D. Kapec, P. Mitra, A.-M. Raclariu, and A. Strominger, Phys. Rev. Lett. **119**, 121601 (2017).
[24] T. He, D. Kapec, A.-M. Raclariu, and A. Strominger, J. High Energy Phys. 08 (2017) 050.
[25] A. Strominger and A. Zhiboedov, J. High Energy Phys. 01 (2016) 086.
[26] S. Pasterski, A. Strominger, and A. Zhiboedov, J. High Energy Phys. 12 (2016) 053.
[27] G. Compère, R. Oliveri, and A. Seraj, J. High Energy Phys. 10 (2020) 116.
[28] G. Barnich and C. Troessaert, J. High Energy Phys. 12 (2011) 105.
[29] E. E. Flanagan and D. A. Nichols, Phys. Rev. D **95**, 044002 (2017).
[30] D. A. Nichols, Phys. Rev. D **95**, 084048 (2017).
[31] K. Mitman, J. Moxon, M. A. Scheel, S. A. Teukolsky, M. Boyle, N. Deppe, L. E. Kidder, and W. Throwe, Phys. Rev. D **102**, 104007 (2020).
[32] K. Mitman *et al.*, Phys. Rev. D **103**, 024031 (2021).
[33] A. C. Jenkins and M. Sakellariadou, Classical Quantum Gravity **38**, 165004 (2021).
[34] M. Mukhopadhyay, C. Cardona, and C. Lunardini, J. Cosmol. Astropart. Phys. 07 (2021) 055.
[35] S. M. Du and A. Nishizawa, Phys. Rev. D **94**, 104063 (2016).
[36] A. Seraj, J. High Energy Phys. 05 (2021) 283.

[37] S. Tahura, D. A. Nichols, and K. Yagi, Phys. Rev. D **104**, 104010 (2021).
[38] S. Hou, T. Zhu, and Z.-H. Zhu, J. Cosmol. Astropart. Phys. 04 (2022) 032.
[39] K. Koyama, Phys. Rev. D **102**, 021502 (2020).
[40] V. B. Braginsky and L. P. Grishchuk, Sov. Phys. JETP **62**, 427 (1985).
[41] B. P. Abbott *et al.* (LIGO Scientific, Virgo Collaborations), Phys. Rev. Lett. **116**, 061102 (2016).
[42] N. Seto, Mon. Not. R. Astron. Soc. **400**, L38 (2009).
[43] R. van Haasteren and Y. Levin, Mon. Not. R. Astron. Soc. **401**, 2372 (2010).
[44] M. S. Pshirkov, D. Baskaran, and K. A. Postnov, Mon. Not. R. Astron. Soc. **402**, 417 (2010).
[45] J. M. Cordes and F. A. Jenet, Astrophys. J. **752**, 54 (2012).
[46] D. R. Madison, J. M. Cordes, and S. Chatterjee, Astrophys. J. **788**, 141 (2014).
[47] Z. Arzoumanian *et al.* (NANOGrav Collaboration), Astrophys. J. **810**, 150 (2015).
[48] P. D. Lasky, E. Thrane, Y. Levin, J. Blackman, and Y. Chen, Phys. Rev. Lett. **117**, 061102 (2016).
[49] L. O. McNeill, E. Thrane, and P. D. Lasky, Phys. Rev. Lett. **118**, 181103 (2017).
[50] A. K. Divakarla, E. Thrane, P. D. Lasky, and B. F. Whiting, Phys. Rev. D **102**, 023010 (2020).
[51] O. M. Boersma, D. A. Nichols, and P. Schmidt, Phys. Rev. D **101**, 083026 (2020).
[52] N. Khera, B. Krishnan, A. Ashtekar, and T. De Lorenzo, Phys. Rev. D **103**, 044012 (2021).
[53] M. Hübner, C. Talbot, P. D. Lasky, and E. Thrane, Phys. Rev. D **101**, 023011 (2020).
[54] M. Hübner, P. Lasky, and E. Thrane, Phys. Rev. D **104**, 023004 (2021).
[55] T. Islam, S. E. Field, G. Khanna, and N. Warburton, arXiv: 2109.00754.
[56] Z.-C. Zhao, X. Liu, Z. Cao, and X. He, Phys. Rev. D **104**, 064056 (2021).
[57] B. P. Abbott *et al.* (LIGO Scientific Collaboration), Classical Quantum Gravity **34**, 044001 (2017).
[58] M. Punturo *et al.*, Classical Quantum Gravity **27**, 194002 (2010).
[59] H. Yang and D. Martynov, Phys. Rev. Lett. **121**, 071102 (2018).
[60] K. Islo, J. Simon, S. Burke-Spolaor, and X. Siemens, arXiv:1906.11936.
[61] J. Luo *et al.* (TianQin Collaboration), Classical Quantum Gravity **33**, 035010 (2016).
[62] J. Mei *et al.* (TianQin Collaboration), Prog. Theor. Exp. Phys. **2021**, 05A107 (2021).
[63] Y.-M. Hu, J. Mei, and J. Luo, Natl. Sci. Rev. **4**, 683 (2017).
[64] H.-M. Fan, Y.-M. Hu, E. Barausse, A. Sesana, J.-d. Zhang, X. Zhang, T.-G. Zi, and J. Mei, Phys. Rev. D **102**, 063016 (2020).
[65] S. Liu, Y.-M. Hu, J.-d. Zhang, and J. Mei, Phys. Rev. D **101**, 103027 (2020).
[66] S. Liu, L.-G. Zhu, Y.-M. Hu, J.-d. Zhang, and M.-J. Ji, Phys. Rev. D **105**, 023019 (2022).
[67] S.-J. Huang, Y.-M. Hu, V. Korol, P.-C. Li, Z.-C. Liang, Y. Lu, H.-T. Wang, S. Yu, and J. Mei, Phys. Rev. D **102**, 063021 (2020).
[68] Z.-C. Liang, Y.-M. Hu, Y. Jiang, J. Cheng, J.-d. Zhang, and J. Mei, Phys. Rev. D **105**, 022001 (2022).
[69] C. Shi, J. Bao, H. Wang, J.-d. Zhang, Y. Hu, A. Sesana, E. Barausse, J. Mei, and J. Luo, Phys. Rev. D **100**, 044036 (2019).
[70] J. Bao, C. Shi, H. Wang, J.-d. Zhang, Y. Hu, J. Mei, and J. Luo, Phys. Rev. D **100**, 084024 (2019).
[71] T.-G. Zi, J.-D. Zhang, H.-M. Fan, X.-T. Zhang, Y.-M. Hu, C. Shi, and J. Mei, Phys. Rev. D **104**, 064008 (2021).
[72] L.-G. Zhu, L.-H. Xie, Y.-M. Hu, S. Liu, E.-K. Li, N. R. Napolitano, B.-T. Tang, J.-d. Zhang, and J. Mei, Sci. China Phys. Mech. Astron. **65**, 259811 (2022).
[73] C. Shi, M. Ji, J.-d. Zhang, and J. Mei, arXiv:2210.13006.
[74] N. Xie, J.-d. Zhang, S.-J. Huang, Y.-M. Hu, and J. Mei, Phys. Rev. D **106**, 124017 (2022).
[75] H.-T. Wang *et al.*, Phys. Rev. D **100**, 043003 (2019).
[76] W.-F. Feng, H.-T. Wang, X.-C. Hu, Y.-M. Hu, and Y. Wang, Phys. Rev. D **99**, 123002 (2019).
[77] M. Favata, Phys. Rev. D **80**, 024002 (2009).
[78] M. Favata, Astrophys. J. Lett. **696**, L159 (2009).
[79] M. Favata, Classical Quantum Gravity **27**, 084036 (2010).
[80] C. Talbot, E. Thrane, P. D. Lasky, and F. Lin, Phys. Rev. D **98**, 064031 (2018).
[81] G. Compère and A. Fiorucci, arXiv:1801.07064.
[82] G. Barnich and C. Troessaert, J. High Energy Phys. 05 (2010) 062.
[83] SXS Gravitational Waveform Database, http://www.black-holes.org/waveforms.
[84] M. Boyle *et al.*, Classical Quantum Gravity **36**, 195006 (2019).
[85] J. Moxon, M. A. Scheel, and S. A. Teukolsky, Phys. Rev. D **102**, 044052 (2020).
[86] N. Ezra and P. Roger, J. Math. Phys. (N.Y.) **3**, 566 (1962).
[87] C. García-Quirós, M. Colleoni, S. Husa, H. Estellés, G. Pratten, A. Ramos-Buades, M. Mateu-Lucena, and R. Jaume, Phys. Rev. D **102**, 064002 (2020).
[88] M. Colleoni, M. Mateu-Lucena, H. Estellés, C. García-Quirós, D. Keitel, G. Pratten, A. Ramos-Buades, and S. Husa, Phys. Rev. D **103**, 024029 (2021).
[89] G. Pratten, S. Husa, C. Garcia-Quiros, M. Colleoni, A. Ramos-Buades, H. Estelles, and R. Jaume, Phys. Rev. D **102**, 064001 (2020).
[90] LIGO Scientific Collaboration, Virgo Collaboration, LALSuite, https://git.ligo.org/lscsoft/lalsuite.
[91] D. J. A. McKechan, C. Robinson, and B. S. Sathyaprakash, Classical Quantum Gravity **27**, 084020 (2010).
[92] M. Maggiore, *Gravitational Waves. Vol. 1: Theory and Experiments*, Oxford Master Series in Physics (Oxford University Press, New York, 2007).
[93] N. Cornish and T. Robson, J. Phys. Conf. Ser. **840**, 012024 (2017).
[94] T. Robson, N. J. Cornish, and C. Liu, Classical Quantum Gravity **36**, 105011 (2019).
[95] D. Kennefick, Phys. Rev. D **50**, 3587 (1994).
[96] A. D. Johnson, S. J. Kapadia, A. Osborne, A. Hixon, and D. Kennefick, Phys. Rev. D **99**, 044045 (2019).
[97] C. Reisswig, S. Husa, L. Rezzolla, E. N. Dorband, D. Pollney, and J. Seiler, Phys. Rev. D **80**, 124026 (2009).
[98] C. O. Lousto, M. Campanelli, Y. Zlochower, and H. Nakano, Classical Quantum Gravity **27**, 114006 (2010).

[99] P. Ajith *et al.*, Phys. Rev. Lett. **106**, 241101 (2011).
[100] L. Santamaria *et al.*, Phys. Rev. D **82**, 064016 (2010).
[101] E. Barausse, Mon. Not. R. Astron. Soc. **423**, 2533 (2012).
[102] A. Sesana, E. Barausse, M. Dotti, and E. M. Rossi, Astrophys. J. **794**, 104 (2014).
[103] F. Antonini, E. Barausse, and J. Silk, Astrophys. J. **812**, 72 (2015).
[104] P. Madau and M. J. Rees, Astrophys. J. Lett. **551**, L27 (2001).
[105] V. Bromm and A. Loeb, Astrophys. J. **596**, 34 (2003).
[106] M. C. Begelman, M. Volonteri, and M. J. Rees, Mon. Not. R. Astron. Soc. **370**, 289 (2006).
[107] G. Lodato and P. Natarajan, Mon. Not. R. Astron. Soc. **371**, 1813 (2006).
[108] L.-G. Zhu, Y.-M. Hu, H.-T. Wang, J.-d. Zhang, X.-D. Li, M. Hendry, and J. Mei, Phys. Rev. Res. **4**, 013247 (2022).
[109] M. Vallisneri, Phys. Rev. D **77**, 042001 (2008).
[110] K. Chatziioannou, A. Klein, N. Yunes, and N. Cornish, Phys. Rev. D **95**, 104004 (2017).
[111] A. Mangiagli, A. Klein, A. Sesana, E. Barausse, and M. Colpi, Phys. Rev. D **99**, 064056 (2019).
[112] E. Baird, S. Fairhurst, M. Hannam, and P. Murphy, Phys. Rev. D **87**, 024035 (2013).
[113] S. van der Walt, S. C. Colbert, and G. Varoquaux, Comput. Sci. Eng. **13**, 22 (2011).
[114] P. Virtanen *et al.*, Nat. Methods **17**, 261 (2020).
[115] J. D. Hunter, Comput. Sci. Eng. **9**, 90 (2007).